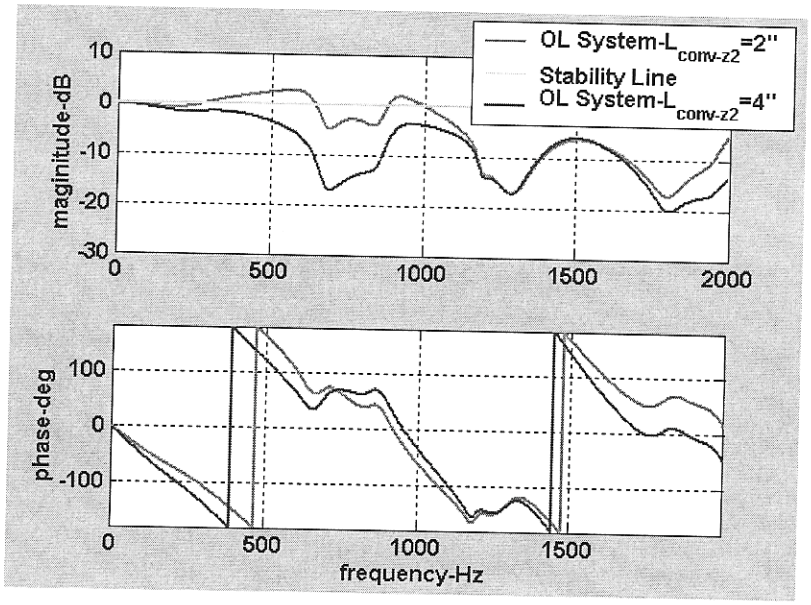

Figure 2.2.11 Thermo-acoustic instability model predictions

Fabricated combustor components were not tested prior to the redirection of the program.

2.3 Organic Rankine Cycle (ORC) Technology Development

Technology for the Organic Rankine Cycle (ORC) system was developed in two stages. The Generation 1 ORC subsystem was primarily a risk reduction activity that was evaluated using a simulated engine exhaust. Subsequently, many of the components were enhanced and integrated into a Generation 2 system that was operated off the exhaust of a 1.2 MW gas turbine.

2.3.1 Generation 1 ORC

The Generation 1 ORC utilized near-off-the-shelf components without modification. For example, the turbine was a Carrier (19XR225) centrifugal compressor running with reverse flow, and the condenser was a pair of Carrier (09DK094) air cooled condensers. The evaporator came from a Carrier supplier.

The 19XR225 is a Carrier centrifugal compressor employing conical diffuser. It is used for water chilling duty of about 225 tons with refrigerant R134a and is as such the smallest compressor in a family of compressors sized for duties up to 1500 tons. Figure 2.3.1 is a cross-section of this compressor. It consists of an induction motor driving the compressor through a gearbox. When the compressor is used as turbine, the high pressure vapor enters what used to be the discharge of the compressor, expands through the turbine, and discharges through what used to be the compressor inlet. The turbine drives the induction generator.

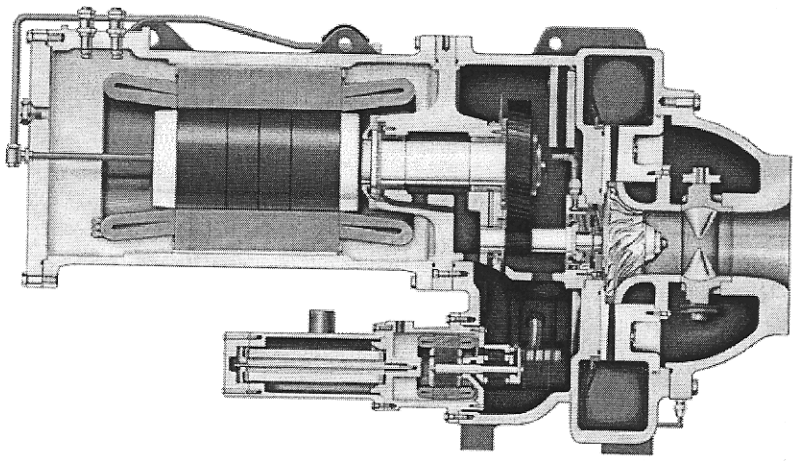

Figure 2.3.1 19XR225 compressor

The condenser used on this ORC was Carrier air cooled condenser shown in Figure 2.3.2. The refrigerant inlet and outlet were modified to match the ORC system. Such condensers are routinely used on many Carrier products and are manufactured in large quantities.

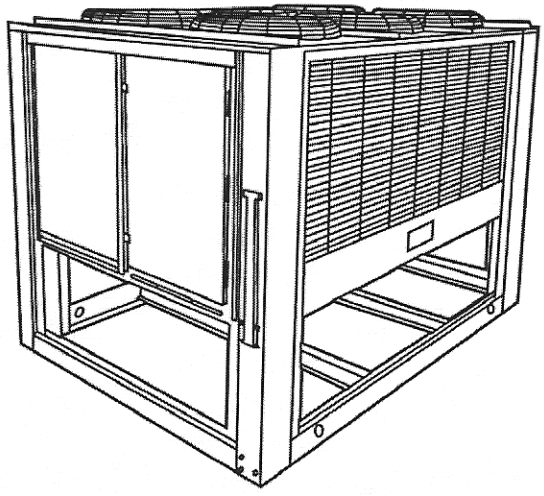

Figure 2.3.2 09DK094 Carrier air cooled condenser

The evaporator shown in Figure 2.3.3 was designed by Carrier and built by a Carrier supplier. It was constructed out carbon steel tubes and fins. The two sections of the evaporator were designed as a counter-flow type and co-flow type. The sub-cooled refrigerant got heated to boiling point in the counter flow section, and further got heated to the turbine inlet condition in the co-flow section.

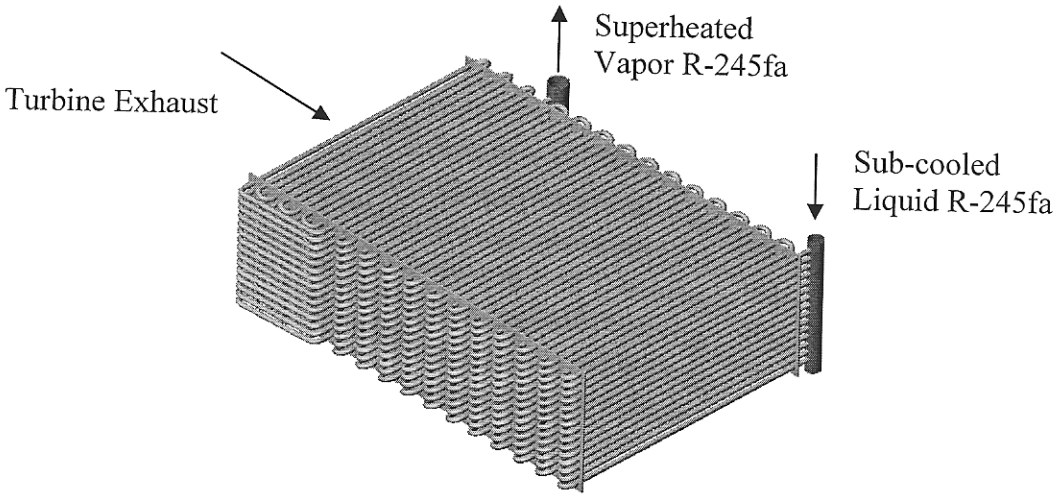

Figure 2.3.3 Gen I ORC evaporator (air ducting not shown)

The test facility shown in Figure 2.3.4 included provision for substantial pressure and temperature instrumentation to measure component overall performance, line losses, component health, and flow distribution for component model validation. The turbine had 30 internal pressure measurements in the shroud and impeller area and 3 exit wedge probes (to measure exit swirl angle) to diagnosis turbine performance. The evaporator and condenser were instrumented with a vast array of thermocouples for performance and heat transfer coefficient calibration. In addition, instrumentation was also in place to measure motor power consumption by the pumps and condenser fans, as well as electrical generator power output. The energy source was a controlled flowrate of electrically-heated air.

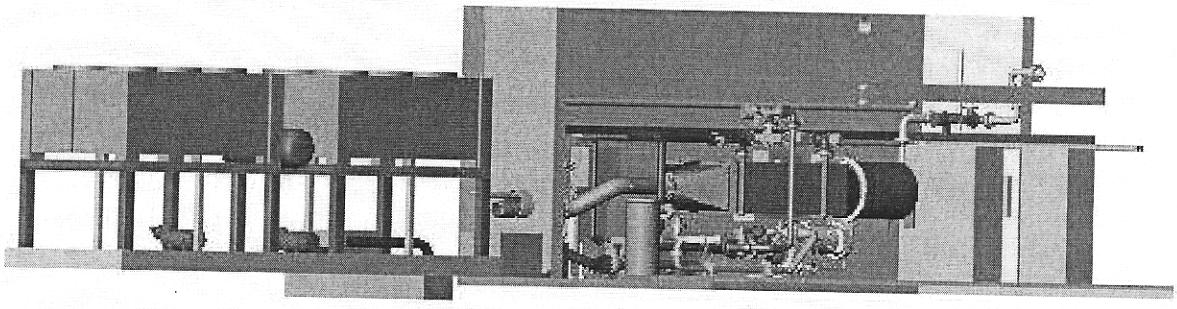

Figure 2.3.4 Gen I ORC test system

The turbine was tested for several hours. A peak electric power output of 64 kW was achieved during these tests, a result consistent with model predictions when using the production compressor impeller and nozzle arrangement. This achievement marked a major milestone on the path to demonstrating 80 kW net power target. Further power increase was expected after the installation of optimized impeller, shroud and nozzle

designs. Behavior of the turbine oil reclaim and motor cooling subsystems was also studied during these tests. Several detail changes were made to these subsystems to properly balance the pressure in the three internal generator and gearbox cavities and thus maintain the appropriate oil and coolant flows. Reliable operation of the bearing/lubrication system was demonstrated except at the highest load conditions. This behavior, which was believed to result from the use of compressor bearings in reverse rotation, was addressed through modification of the original tilt-pad bearing.

Heat exchanger performance was verified. The vapor generator was to deliver 7 lb/s of R245fa with 20F superheat from a 700F, 5 lb/s inlet air stream with minimal allowable air-side pressure drop. The model accurately predicted the vapor generator capacity. The measured air-side temperature drop was predicted to within <1%. The R245fa side was also well predicted. Figure 2.3.5 shows a side view of the vapor generator, followed by the measured row-by-row temperature profile in the middle tube sheet and the model tube sheet average temperature prediction. (Note that the physical evaporator is counter-flow until row 24 and then co-flow to the exit at row 30. For clarity, the plotted temperature profiles are shown as if the entire unit was counter-flow.) The model followed the measured profile closely, and predicted a final superheat between the measured middle tube sheet value and the mixed superheat measured in the outlet header. Some vertical mal-distribution of outlet superheat was noted, apparently caused by gravity effects. Pressure drop on both air and R245fa sides was under predicted by 10-20%, but the as-tested values were acceptably low.

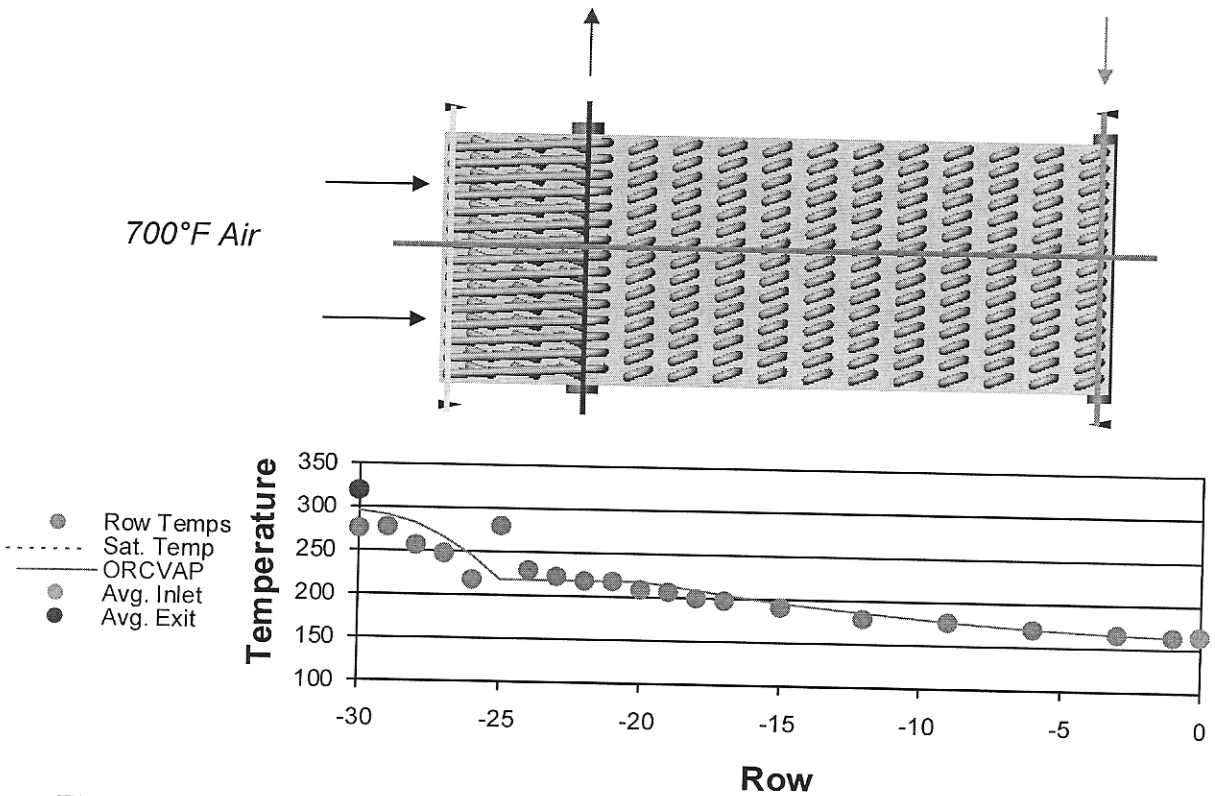

Figure 2.3.5 Gen I ORC evaporator performance

The condenser had to reject 700 kW of energy with a saturation temperature no more than 36F above the ambient to achieve the design turbine pressure ratio. Condenser capacity was measured to be 5-10% greater than model predictions. On the other hand, the saturation temperature limit was not achieved. Although the condenser coil pressure drop was well predicted, the overall condenser inlet pressure, and thus saturation temperature, was under-predicted due to excessive friction losses in the standard condenser inlet manifolds and buildup of non-condensable gases in the receiver tank. This indicated a need to implement a large size condenser inlet manifold to reduce the line loss and a purge mechanism to control the non-condensable. Finally, the 350 kW feed-heaters performed very well. Measured capacities on both sides were consistent to within 10% of design. Vapor-side pressure drop measurements exceeded the design value, but this was consistent with operation of the system at more than design superheat.

Pump performance was sufficient to support system testing, but improvements were clearly necessary to demonstrate technical readiness. The procured variable-speed pump showed a propensity to cavitate at half the nominal impeller speed when supplied with effectively saturated liquid at the specified net pump suction head (NPSH). Using two similar pumps in series allowed the first pump to be operated at low speed, and thus low pressure rise, without cavitation. Full speed operation of the downstream pump then delivered the required system pressure without cavitation because of the increased NPSH provided by the upstream pump. Control of the system flow currently required manual throttling, which dissipated a large amount of energy. The system was not efficient, but was fully functional. In subsequent tests however, the second pump was equipped with a variable speed drive to replace the throttle valve, improving efficiency and enabling tests of automatic superheat control algorithms.

2.3.2 Component Modifications

2.3.2.1 Aerodynamic Enhancements

A one-dimensional meanline model of the nozzle, gap, and impeller, as well as a three-dimensional CFD model of the nozzle and gap, were developed to improve the design of these critical components. CFD model results comparing Mach number in the nozzles and gap for cases with eight and sixteen azimuthal nozzles are shown in Figure 2.3.6. The actual final design configuration was selected to achieve the target 80% efficiency.

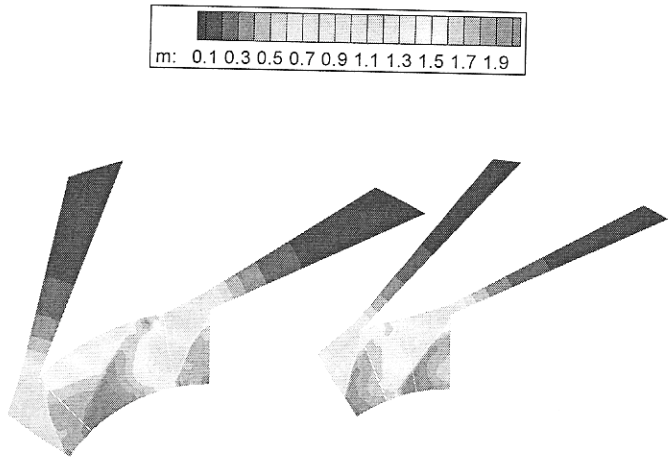

Figure 2.3.6 Mach number profiles for the turbine nozzles and gap.

2.3.2.2 Generator Drive-System Enhancements

Two issues involving the turbo-generator bearings and system oil management were identified that related to reversing the gas flow through the impeller. The thrust bearing for the impeller shaft, a tilt-pad unit designed for rotation in a compressor, could not support full design power over a long-term when rotating in the opposite direction. The bearing pads could be modified to tilt the opposite direction for improved power operation. However, analysis showed that the modified bearing would be marginal during a loss-of-power transient because the impeller coast is longer in turbine mode. For this reason, and to reduce turbo-generator mechanical losses by an estimated 6 kW, rotating element bearings were designed and incorporated. The design drawing is shown in Figure 2.3.7.

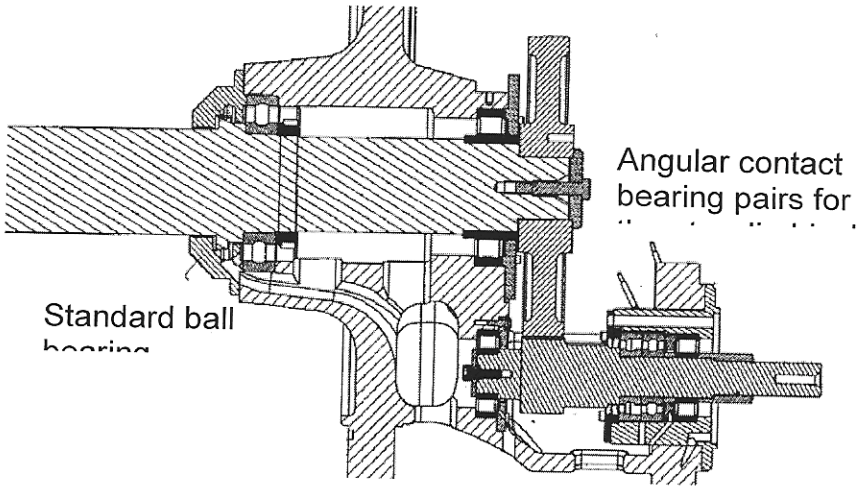

Figure 2.3.7 Turbine impeller and generator shafting with roller element bearings.

Motor cooling and oil management in the motor/compressor unit required careful balancing of pressures in its three internal cavities. In addition, lubricant thermal stability testing was completed. Figure 3.2.4.8 shows oil samples maintained at 212F for several weeks without metals and at 392F with metals. Clearly, the oil stability is affected at the higher temperature in the presence of metals. Passivating the metal surfaces allows long-term operation at 347F without loss of stability.

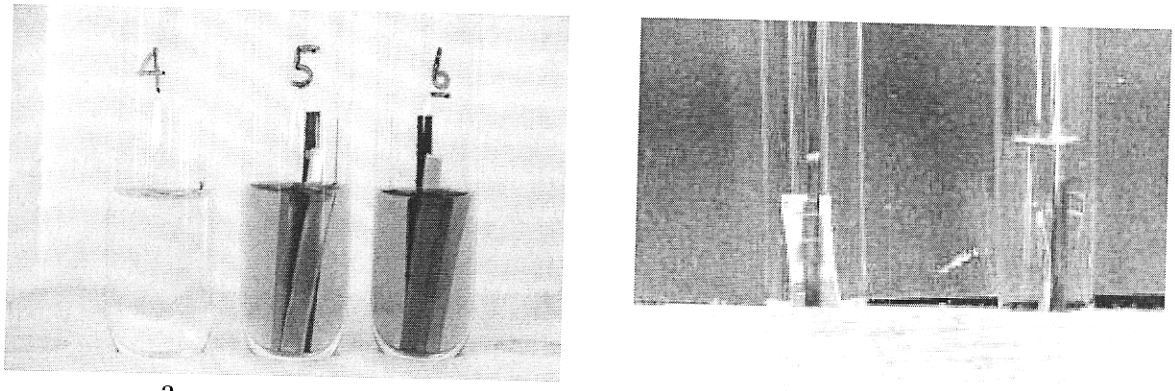

a. b.

Figure 2.3.8 Long-term lubricant stability test results

2.3.2.3 Motor and oil cooling system modifications

The interdependent oil management and motor cooling systems were completely redesigned. Earlier testing was often limited by significant losses of oil from the gearbox sump. These losses primarily occurred when initiating turbine operation from turbine bypass, and when the motor cooling system was manually actuated. Analysis of the system data showed that large pressure differences could occur between the motor cavity and the transmission cavity in these circumstances, causing ejection of bearing lubrication oil into the motor casing and subsequently into the system. Also, with a single coolant stream feeding the motor and oil cooler in series, we found it difficult to get the correct balance between cooling loads. To resolve these problems, the cooling system was revised to feed the motor and oil cooling loads in parallel. These cooling circuits are illustrated in Figure 2.3.9.

Management of oil inventory during transients was determined to be primarily an operational issue. To study this problem in more detail, a sophisticated UV spectrophotometer system was installed to measure oil concentration at the refrigerant-pump outlet as a function of time. Oil losses can now be correlated with all other system data, allowing diagnosis and control of the phenomenon shown below in Figure 2.3.10.

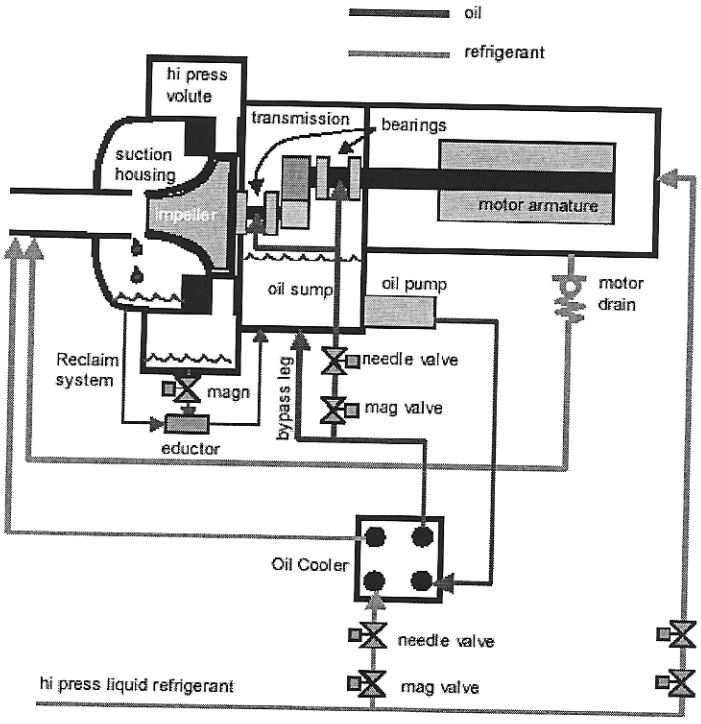

Figure 2.3.9 Motor & oil cooling circuits and oil management system

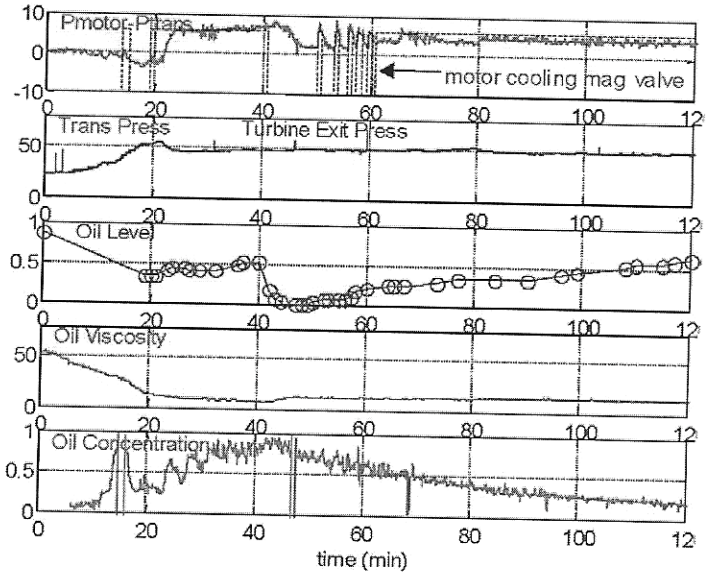

Figure 2.3.10 Motor and oil cooling circuit performance

Figure 2.3.10 shows representative test data that was recorded during the development phase of the oil/motor cooling system. In this series of plots, the system heat-up begins at approximately 5 minutes, reaching equilibrium at about 40 minutes. The circulating oil concentration rises during this time while the oil level drops and then stabilizes when

motor cooling is initiated at 20 minutes, pressurizing the motor cavity and arresting the loss of oil from the transmission cavity. At 40 minutes, overcooling of the motor cavity required that motor cooling be discontinued, whereupon the motor cavity pressure and the oil level dropped dramatically. The oil eductor system was started approximately 42 minutes into the plot when the hot gas temperature was sufficiently high, and both oil concentration and level responded favorably within 2-3 minutes. Motor cooling was adjusted several times between 50 and 60 minutes until the correct flow rate was achieved. Once motor cooling was restored, oil was reclaimed steadily over the next hour while good motor temperature was maintained. Oil viscosity also rises and stabilizes over this time, demonstrating good control of oil temperature and refrigerant concentration in the oil sump.

Operation of the ORC with this revised oil management system, without the oil separator, showed that our current ORC startup sequence minimized the loss of oil from the turbo-generator sump. Also, the eductor system was able to restore the circulating oil concentration to an acceptable level over about an hour of operation.

2.3.2.4 Condenser modifications

Condenser coil capacity was well predicted by models, but the condensing temperature was higher than anticipated. This higher condensing temperature reduced the pressure ratio across the turbine and consequently the work that could be extracted from it. Analysis of the data, summarized in Fig. 3.2.4.12, shows that a larger than expected pressure drop in the condenser inlet manifold, combined with collection of non-condensable gases in the system, accounted for the high condensing temperature. The manifold design was revised to reduce vapor velocities and to trap any liquid R245fa condensed on the vapor line walls. Also, commercial refrigerant purge units were evaluated for their applicability to R245fa and got incorporated in the system.

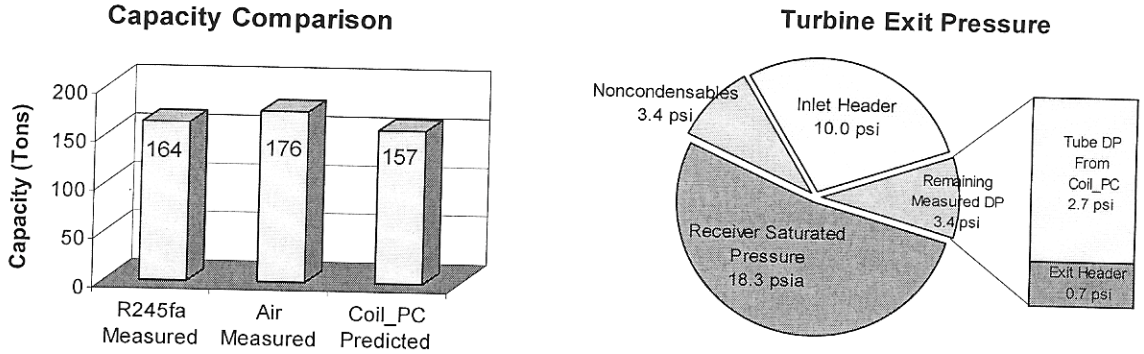

Figure 2.3.11 Validation of condenser capacity and pressure drop

2.3.2.5 Pump Enhancements

A major contributor to pump cavitation was entrainment of vapor bubbles from the receiver at low fluid level operations. The condenser return lines were initially routed into the vapor space of the tank, causing considerable frothing. These lines were later extended to the bottom of the tank to prevent condensation in the vapor space and to minimize frothing. This was effective until the receiver level dropped below a certain level, when the returns would uncover and entrain vapor into the remaining liquid. Any bubbles sucked into the pump inlet would not have time to condense in the near-saturation liquid, and cavitation would occur. A sparger was developed to slow the flow velocity and thus greatly minimize this entrainment.

Regardless of the receiver design, the provided NPSH could not support full flow without the use of a boost pump. Because non-condensable gases are continuously purged from the system, it appeared likely that the pump inlet fluid was simply too close to saturation. Increasing the physical pump suction head was not feasible, but it was possible to add a small water-cooled heat exchanger to give a few degrees more sub-cooling to the nearly saturated fluid entering the pump. Testing showed that the combination of spargers and sub-cooling allowed operation of the system at full capacity without the boost pump. Also, sensitivity of the pump to rapid condenser fan variations appeared decreased.

However, effect of low available NPSH was persistent and the pump cavitated readily. Secondly, since the characteristic curve of the pump was practically horizontal, little change in pressure difference across the pump resulted in large swings in flow rate making control of the system exceedingly difficult. The problem was eradicated only after the introduction of a regenerative pump with a steep characteristic curve albeit with poorer efficiency.

2.3.2.5 Electrical Interconnection

In the Generation 1 ORC, the induction generator was connected to the grid through an inverter. In the Generation 2 design, the generator should be connected directly through contactors. In the event that the generator is disconnected from the grid due to a fault trip, the turbine will over-speed to approximately 1.6 times its nominal design speed. The Generation 1 design experienced this phenomenon several times without any apparent damage; however, to avoid potential reliability issues a scheme has been developed to prevent the over-speed condition.

An electrical break was designed to hold the induction motor at close to its nominal operational speed for more than 5 seconds to give the controller time to close the turbine inlet valve and open the bypass valve. The electrical break is shown in Figure 2.3.12.

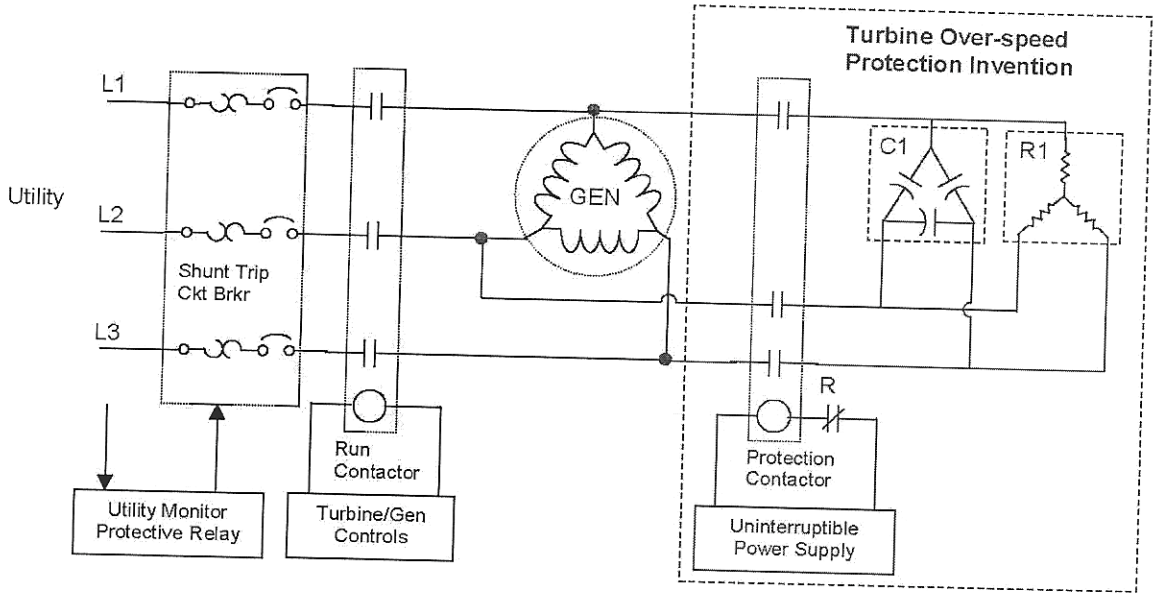

Figure 2.3.12 Over-speed protection scheme

2.3.3 Generation 2 ORC

A 100 kW Generation 2 ORC was assembled and installed at the UTRC Jet Burner Test Stand (JBTS). This site was selected because the JBTS has a 1.2 MW gas turbine engine that could provide the waste heat energy for the ORC. Figure 2.3.13 shows the placement of the ORC at the JBTS. The evaporator was located on the roof of the JBTS where the engine exhaust was available, with insulated pipes for the liquid and vaporized refrigerant. The figure also shows a photograph of the assembled ORC. All of the ORC enhancements described above were implemented in the Generation 2 system. Overall, the unit met all of its requirements. It achieved the design net power of 100 kW, and the turbine met the expected 80% isentropic efficiency. The evaporator, condenser and receiver also performed according to design requirements.

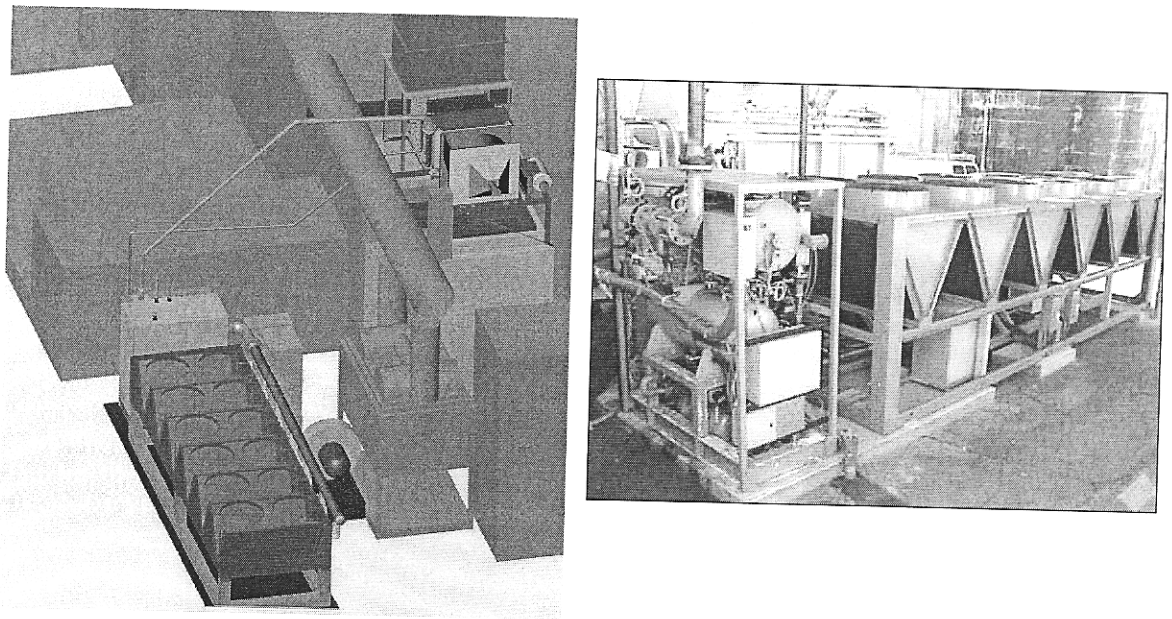

Figure 2.3.13 Generation 2 ORC

The ORC closed-loop control system was further developed during the Generation 2 testing. Throughout the system-operating envelope the following criteria were the guide to develop the control system:

1. The maximum pressure limit must not be exceeded,
2. The maximum temperature limit must not be exceeded, and
3. The superheat must not approach zero
4. It must allow for a smooth system startup and
5. It must allow for safe shutdown if loss of generator power or heat source is sensed.

The evaporator exit condition (turbine inlet) must be maintained in the zone shown in Figure 2.3.14 for reliable operation.

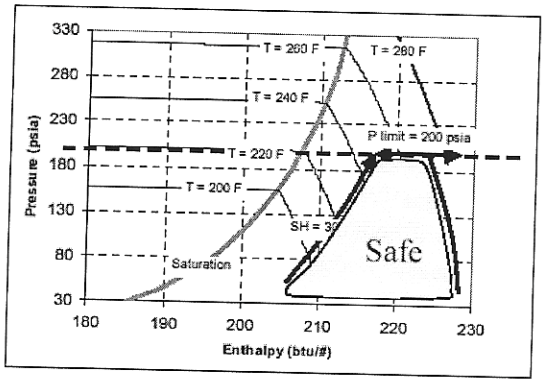

Figure 2.3.14 Safe Turbine Operating Zone

The maximum pressure limit defining the zone is dictated by mechanical strength of the hardware. The maximum temperature limit is dictated by allowable oil temperature. The minimum superheat requirement is imposed to protect the turbine from ingesting liquid for fear of erosion. In addition to the above criteria, the controls must drive the operation state to the high-pressure limit in order to maximize the power efficiency of the system. To achieve these goals a modified-cascade closed loop control scheme was implanted as shown in Figure 2.3.15.

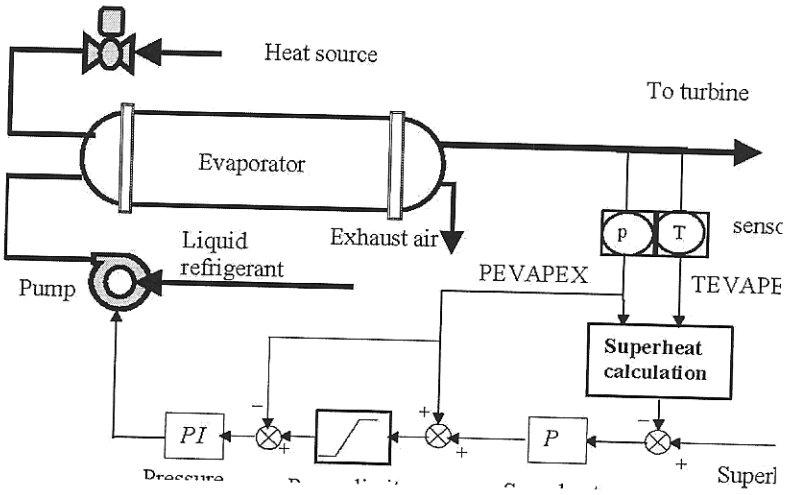

Figure 2.3.15 Modified-cascade closed loop controller.

Using this control scheme there are three modes of operation possible:

- Closed loop PID on superheat,
- Closed loop PID on pressure, and
- Open loop on pump speed.

When in closed loop the pressure/superheat transition occurs seamlessly. When in open-loop the algorithm is not called, and the pump speed is held constant or set by other logic.

The refrigerant pump, which is the primary superheat-control actuator, is designed by the manufacture to be used as a nearly constant-pressure source, in that for a given speed it provides a large range of flow at nearly constant pressure. Using the cascade control scheme, the pressure limits may be varied dynamically to move the system operation from one region to another. The startup scheme transitions from open loop to closed loop, and then varies the pressure limits to slowly increase the operation pressure. The time constant of the pressure loop is fast, which prevents pressure over-shoot. The startup sequence is:

- Apply hot air to evaporator (approximately half the design enthalpy flux)
- Turn on pump to minimum speed (20 Hz).
- Set high pressure limit to a value of pressure that can be achieved at steady-state at the initial low pump speed. (70 psia)
- Wait until operating condition is on the pressure plateau of the pump curve, as determined by a model.

- Ramp up the pressure limit to its normal value (currently 280 psia). At some level the mode will switch from pressure control to superheat control.
- Increase (and control) hot air enthalpy flux to bring the system to full load (maximum pressure and temperature at the evaporator exit).

In the process of testing for reliability, however, four new major problems emerged.

- First, the lack of sufficient NPSH caused the centrifugal pump to cavitate frequently. Sudden change in ambient temperature or sudden increase in the condenser fan speed starved the receiver of refrigerant and subsequently also cavitated the pump. To make things worse, the horizontal shape of the pump's characteristic curve gave the controller a challenge to keep the unit running.
- Second, small pieces of hardened metals such as weld slag, copper and aluminum shavings, bombarded the rotor and nozzle during operation and caused it to fail mechanically. Once the debris reached the area between the rotor and the nozzle, it had no means to exit and therefore, repeatedly damaged both the nozzle and the rotor.
- Third, the match between the natural frequencies of the rotor blades and the second harmonics of the pressure field created by the number of stators, rotor blade number, and the angular velocity of the rotor combinations, caused the rotor to break up.

Each one of these problems were thoroughly analyzed, their root cause were well identified and finally solved and retested on the Generation 2 ORC.

- The solution for the pump problem was to use a regenerative pump instead of a centrifugal pump. Although the efficiency of this pump is slightly inferior, its robust operation under cavitating condition and its low NPSH requirement made it an ideal solution to the problem at hand. Even more attractive is the shape of the characteristic curve of the regenerative pump. The monotonically negative slope made system operation very stable.
- The FOD problem was challenging. . At first it was believed that debris could be filtered out during the commissioning process. However, it was determined that the debris could be introduced during field service operation. Therefore a commissioning filter became permanent.
- A more thorough calculation identified the high cycle fatigue failure problem at the high end of the frequency range. Prior Carrier experience for the turbomachinery used as a compressor did not require this process. The problem was solved by detuning the impeller's natural frequency in a redesign process.

These solutions were all implemented on the Generation 2 ORC which was successfully tested for over 1000 hours.

Section 3.0 Integration and Test of Advanced Microturbine System

The object was to achieve 40% electrical efficiency (LHV at ISO day) from an AMS that consisted of two Capstone C200 microturbines integrated with a water-cooled condenser ORC bottoming system. Two C200 Beta units (identified as unit #3 or #4) were received in late 2004 while UTRC provided the ORC.

3.1 System Integration, Installation, and Instrumentation

A test site at the UTRC CHP Laboratory was prepared for the integrated AMS system. Two C200 engines were mounted on an external concrete pad, with the manifolded exhaust ducted to the evaporator mounted on the CHP Laboratory roof. The top, left image of Figure 3.1.1 depicts the pad and the junction box for the C200 electrical power. The bottom, left image shows the evaporator. The right side of the figure shows the turbine, ORC recuperator, refrigerant pump and pump inverter mounted on the condenser inside the CHP Laboratory. The system was instrumented according to the PID of Figure 3.1.2. The ORC was instrumented exhaustively to calculate the turbine aerodynamic efficiency, condenser performance, evaporator performance, pump performance and recuperator performance. This figure shows that the ORC evaporator exhaust was coupled to a blower on the down-stream side. The blower was turned on or off or its speed was adjusted to set various levels of system backpressure. The entire exhaust assembly, including the evaporator, was insulated to minimize heat loss.

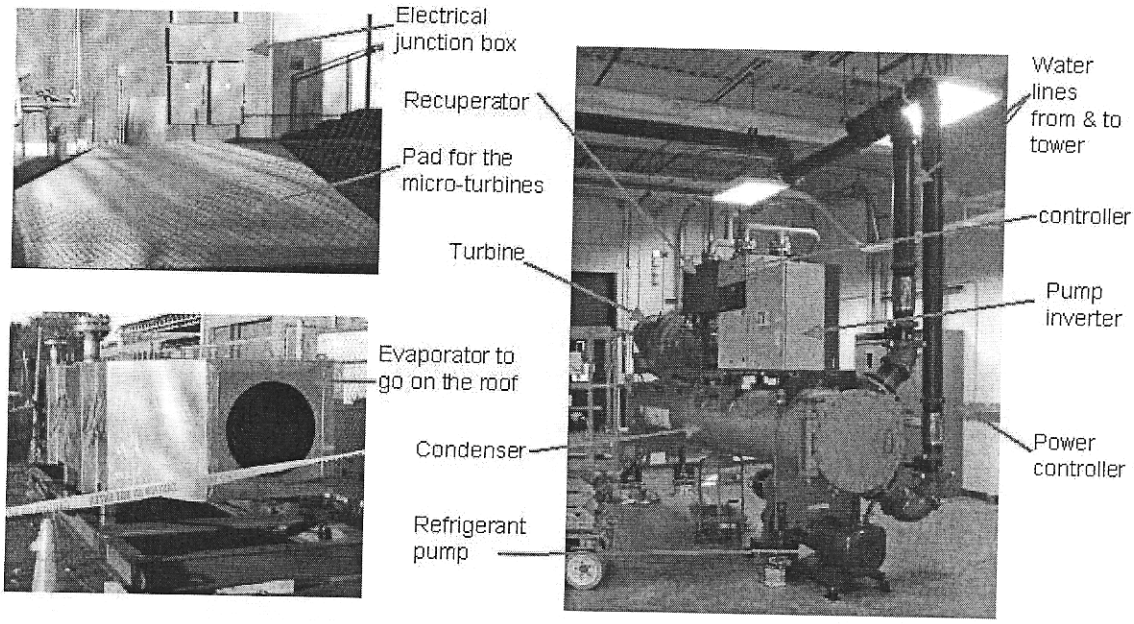

Figure 3.1.1 Installation and integration of C200/ORC AMS

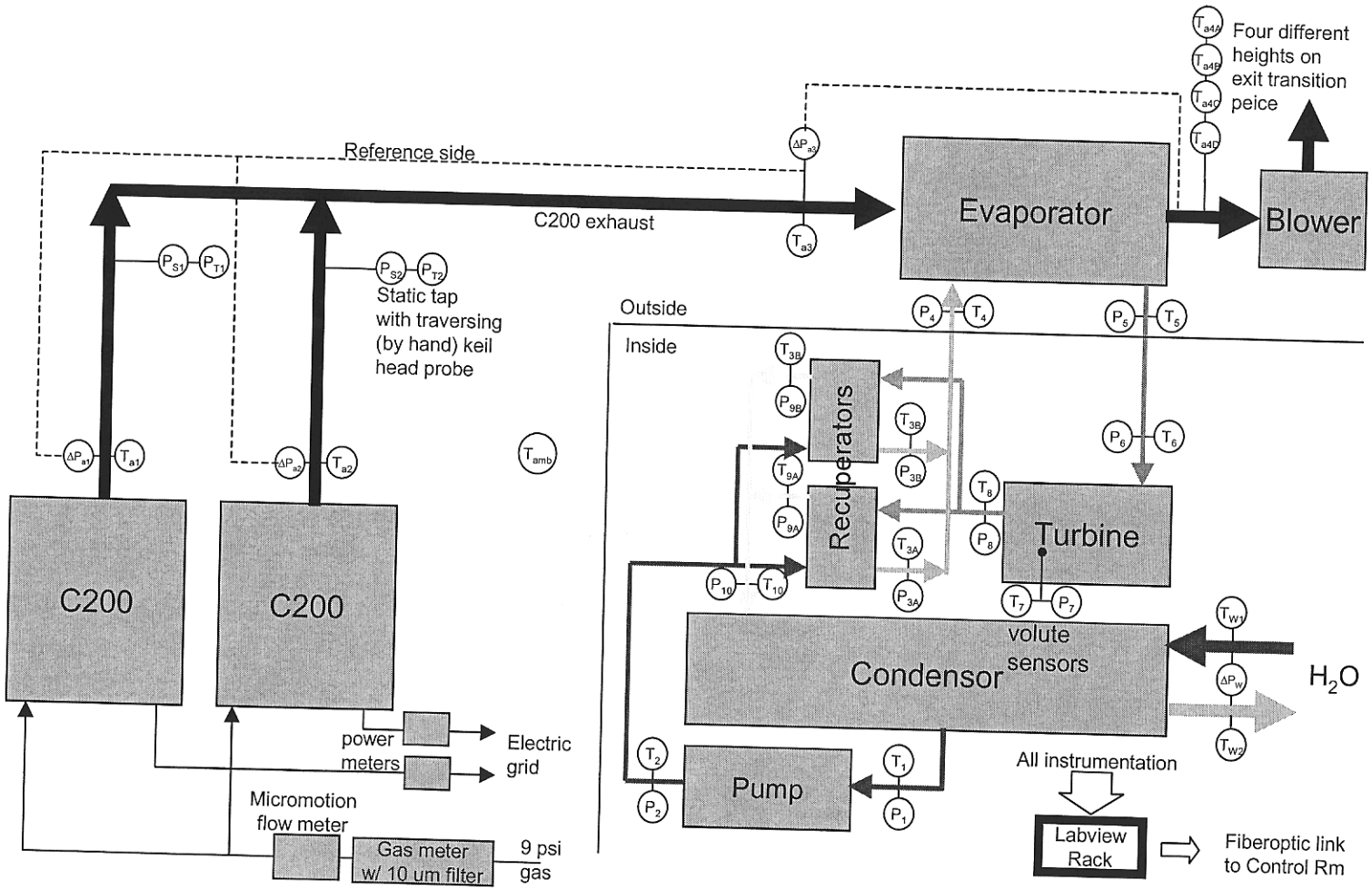

Figure 3.1.2 Instrumentation for integrated C200/ORC AMS

2008 Images Courtesy of www.InfinityTurbine.com - TITLE: Advanced Microturbine Systems - Prepared for US DOE Award No. DE-FC26-OOCH11060 Report Number DOE/CH/11060-1

Data were acquired to characterrize each microturbine and the ORC components. It became apparent that characterizing the C200 electrical power, exhaust energy, and energy losses from the C200 cabinet was important. Individual electrical power meters were used for each microturbine, and the exhaust energy was determined from individual measurements of temperature and flow at the locations shown in Figure 3.1.3. Also indicated are the two roof vents on each microturbine enclosure. Internal blowers draw outside air through the electronic or engine compartments and discharge it through the respective vent. Energy loss through the vents was calculated from integrating temperature and velocity measurements made over the vent exit area.

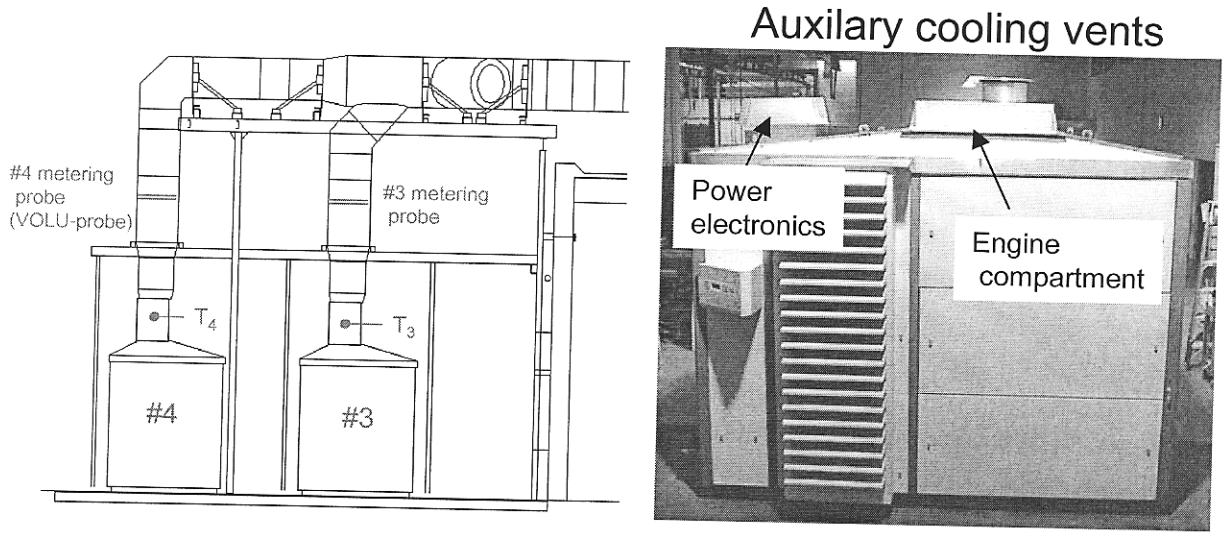

Figure 3.1.3 Microturbine measurements for exhaust and lost energy

3.2 C200 Performance

Figure 3.2.1 plots C200 electrical efficiency data for a modest range of ambient temperature and backpressure. Both plots include the predictions of the same according to Capstone's Design Review document. In the first plot, the data show that the turbine efficiency is 33 % at about 37F ambient temperature without backpressure. This is very consistent with prediction. Efficiency levels with backpressure were reduced by ½%.

The second plot recasts the same data according to backpressure. The 4 to 5 in H2O positive backpressure variation was achieved by varying the blower speed. The prediction for loss of efficiency with backpressure is extremely accurate.

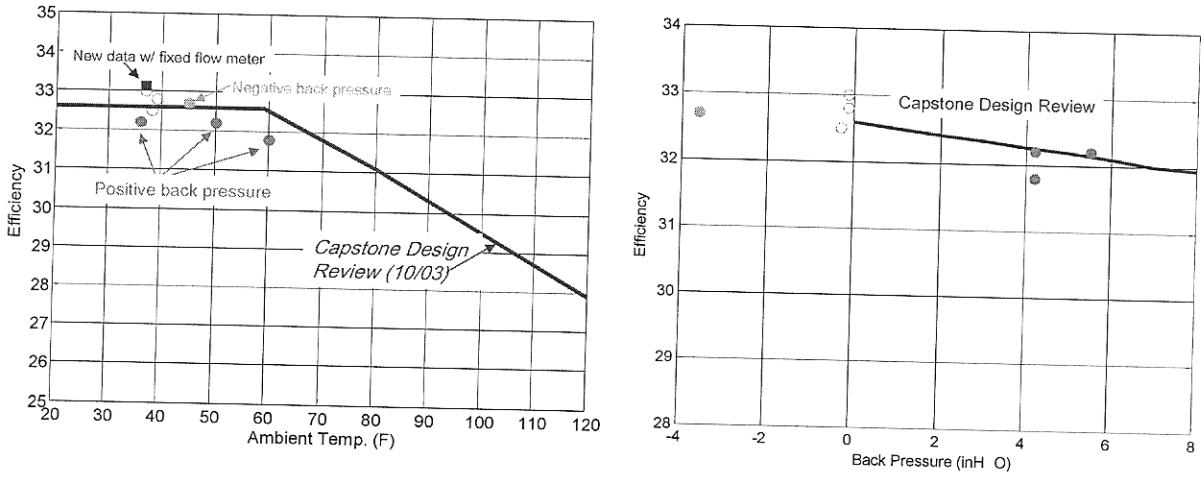

Figure 3.2.1 C200 electrical efficiency

Although the efficiency of the C200 was accurately predicted, the parasitic losses were grossly underestimated, resulting in an over-prediction of the available exhaust energy. As stated above, the turbine enclosure has two major chambers that require adequate ventilation - the engine and the electronics. External air is sucked through the louvers and circulated through these chambers and blown out through the cooling vents. Measurements were conducted on two different days to survey the amount of heat rejected through these vents. A systematic grid was laid out defining a control surface. At each grid point, the temperature and the air velocity was measured and the heat flux through the control surface was then calculated. These surveys indicated that 52kW of energy was lost from microturbine # 4 and 57 kW was lost from microturbine #3 for a total loss of 109 kW. Table 3.2.1 and Table 3.2.2 below show sample data and the corresponding calculation used to determine the heat loss through the cooling vents. In addition thermal energy was lost through natural convection from the enclosure surfaces. The surface temperature was measured to estimate the lost heat by natural convection. It was determined that each unit lost 17 kW by this process. Therefore the total heat loss from both mechanisms was 143 kW.

Table 3.2.1 Energy losses from C200 #4

2/17/05, Heat Leaving Auxilary Cooling Duct of C200 #4 is 32 kW

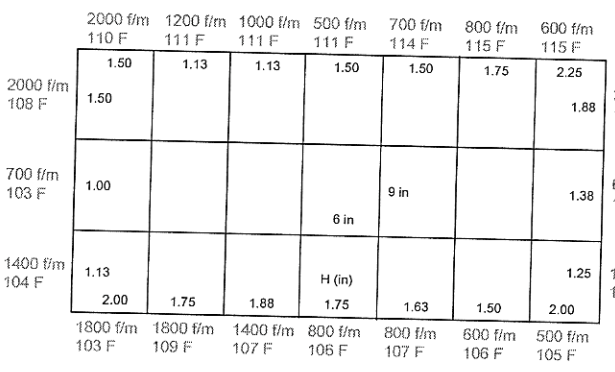

Pamb	14.7	psia		
Tamb	44	F		
Flow rate (f/m)	Temp (F)	Area (sq. in)	rho (slug/ft3)	Power (kW)
2000	110	9	0.00216	2.7
1200	111	6.75	0.00216	1.2
1000	111	6.75	0.00216	1.0
500	111	9	0.00216	0.7
700	114	9	0.00215	1.0
800	115	10.5	0.00214	1.3
600	115	13.5	0.00214	1.3
300	116	16.92	0.00214	0.8
600	128	12.42	0.00210	1.3
1000	122	11.25	0.002118	1.9
500	105	12	0.002182	0.8
600	106	9	0.002178	0.8
800	107	10.5	0.002174	1.2
800	106	10.5	0.002178	1.2
1400	107	11.28	0.002174	2.3
1800	109	10.5	0.002167	2.8
1800	103	12	0.00219	2.9
1400	104	10.17	0.002186	2.0
700	103	9	0.00219	0.9
2000	108	13.5	0.002171	3.9
			total	32.0

2/04/05: Electronics cooling duct of C200 # is ~ 20 kW

Table 3.2.2 Energy losses from C200 #3

2/17/05: Heat Leaving Auxilary Cooling Duct C200 #3 is 31 kW

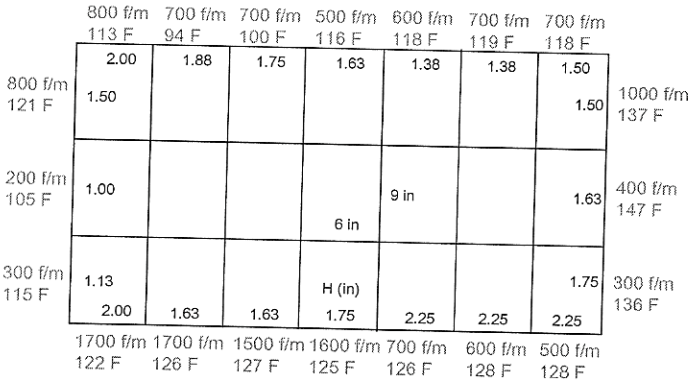

Pamb	14.7	psia		
Tamb	37	F		
Flow rate (f/m)	Temp (F)	Area (sq. in)	rho (slug/ft3)	Power (kW)
800	113	12.0	0.00215	1.5
700	94	11.3	0.00223	0.9
700	100	10.5	0.00220	1.0
500	116	9.8	0.00214	0.8
600	118	9.8	0.00213	1.0
700	119	8.3	0.00213	1.0
700	118	9.0	0.00213	1.0
1000	137	13.5	0.00207	2.6
400	147	14.7	0.00203	1.2
300	130	15.8	0.00209	0.9
1700	122	12.0	0.00212	3.5
1700	126	9.8	0.00210	2.9
1500	127	9.8	0.00210	2.6
1600	125	10.5	0.00211	2.9
700	126	13.5	0.00210	1.7
600	128	13.5	0.00210	1.5
500	128	13.5	0.00210	1.2
300	115	10.2	0.00214	0.5
200	105	9.0	0.00218	0.3
800	121	13.5	0.00212	1.8
			total	30.7

2/04/05: Electronics cooling duct C200 #3 is ~ 26 kW

Figure 3.2.2 shows the measured temperature and flowrate of the C200 exhaust energy. The measured C200 exhaust temperature was at least 35F below expectation from the Capstone Design Review predictions. The exhaust flow rate was also lower than predicted by 6%.

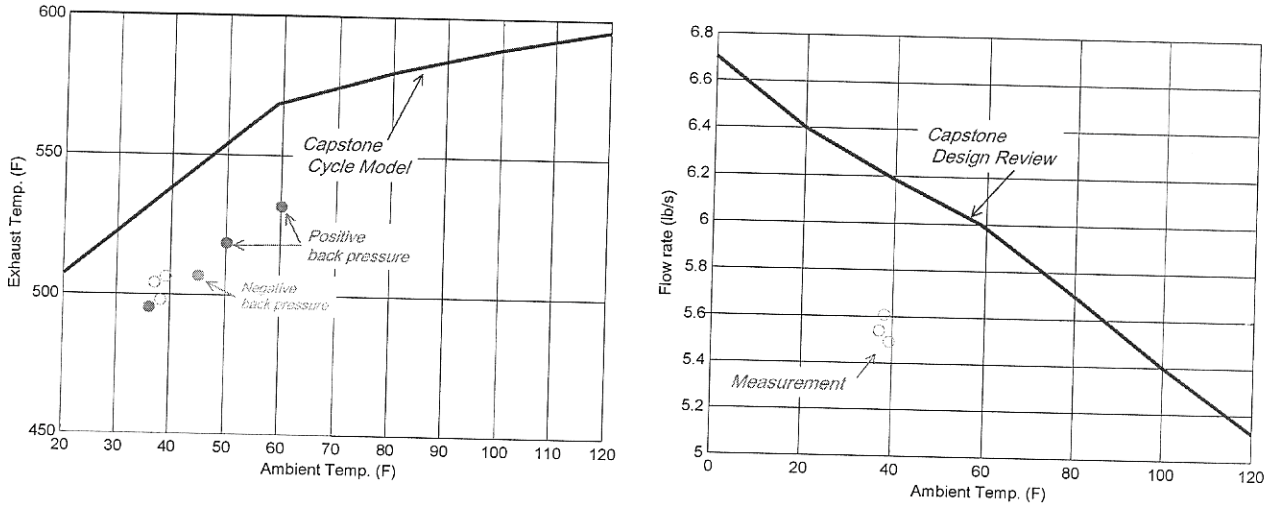

Figure 3.2.2 Measured C200 exhaust characteristics

As a result of all of these deficiencies, the total heat delivered to the ORC evaporator was approximately 150 kW lower than expected based on predictions of exhaust properties. This deficient was consistent with the energy losses described above, providing a very reasonable energy balance of the input fuel energy.

3.3 ORC System Performance

Figure 3.3.1 is a design point calculation summary of the ORC system. In this case, it was assumed that the exhaust temperature of the Capstone 200, or the input temperature of the hot gas to the evaporator of the ORC, would be 568F and that the gas flow of the same stream would be 6 lbm/s, values consistent with the C200 predictions.

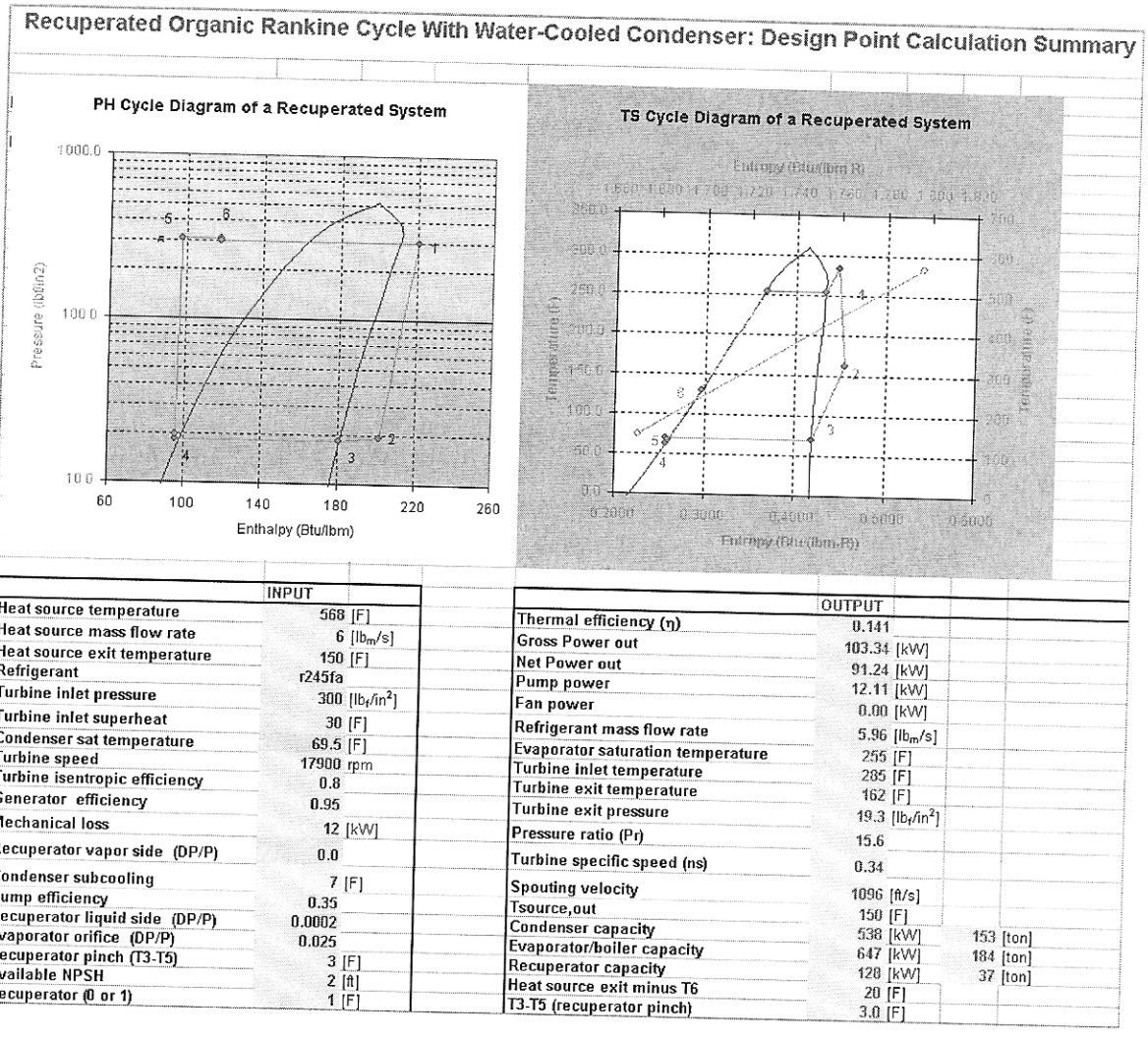

INPUT	
Heat source temperature	568 [F]
Heat source mass flow rate	6 [lb_m/s]
Heat source exit temperature	150 [F]
Refrigerant	r245fa
Turbine inlet pressure	300 [lb_f/in^2]
Turbine inlet superheat	30 [F]
Condenser sat temperature	69.5 [F]
Turbine speed	17900 rpm
Turbine isentropic efficiency	0.8
Generator efficiency	0.95
Mechanical loss	12 [kW]
Recuperator vapor side (DP/P)	0.0
Condenser subcooling	7 [F]
Pump efficiency	0.35
Recuperator liquid side (DP/P)	0.0002
Evaporator orifice (DP/P)	0.025
Recuperator pinch (T3-T5)	3 [F]
Available NPSH	2 [ft]
Recuperator (0 or 1)	1 [F]

OUTPUT		
Thermal efficiency (η)	0.141	
Gross Power out	103.34 [kW]	
Net Power out	91.24 [kW]	
Pump power	12.11 [kW]	
Fan power	0.00 [kW]	
Refrigerant mass flow rate	5.96 [lb_m/s]	
Evaporator saturation temperature	255 [F]	
Turbine inlet temperature	285 [F]	
Turbine exit temperature	162 [F]	
Turbine exit pressure	19.3 [lb_f/in^2]	
Pressure ratio (Pr)	15.6	
Turbine specific speed (ns)	0.34	
Spouting velocity	1096 [ft/s]	
Tsource,out	150 [F]	
Condenser capacity	538 [kW]	153 [ton]
Evaporator/boiler capacity	647 [kW]	184 [ton]
Recuperator capacity	128 [kW]	37 [ton]
Heat source exit minus T6	20 [F]	
T3-T5 (recuperator pinch)	3.0 [F]	

Figure 3.3.1 Predicted ORC design point performance

The output section of the model shows all the predictions. The net power calculated here had allowances for additional mechanical losses in the drive system when we increase the speed for the high pressure-ratio application. It was estimated that the turbine inlet pressure would be 300 lbf/in2 and the condensing temperature would be 69.5F, consuming 647 kW (184 ton) of the heat in the exhaust flue and reject 538 kW (153 ton) of the heat to the condenser. The gross generated power is 103 kW.

Figure 3.3.2 below shows ORC system data when driven by the C200 exhaust. The gross electrical output was 72 kW that is debited by the refrigerant pump power of 8.5 kW, yielding a net power of 63.5 kW. This power was generated with turbine inlet pressure of 212 lbf/in2, much lower than the 300 lbf/in2 predicted by the above model because of the reduced C200 available exhaust energy.

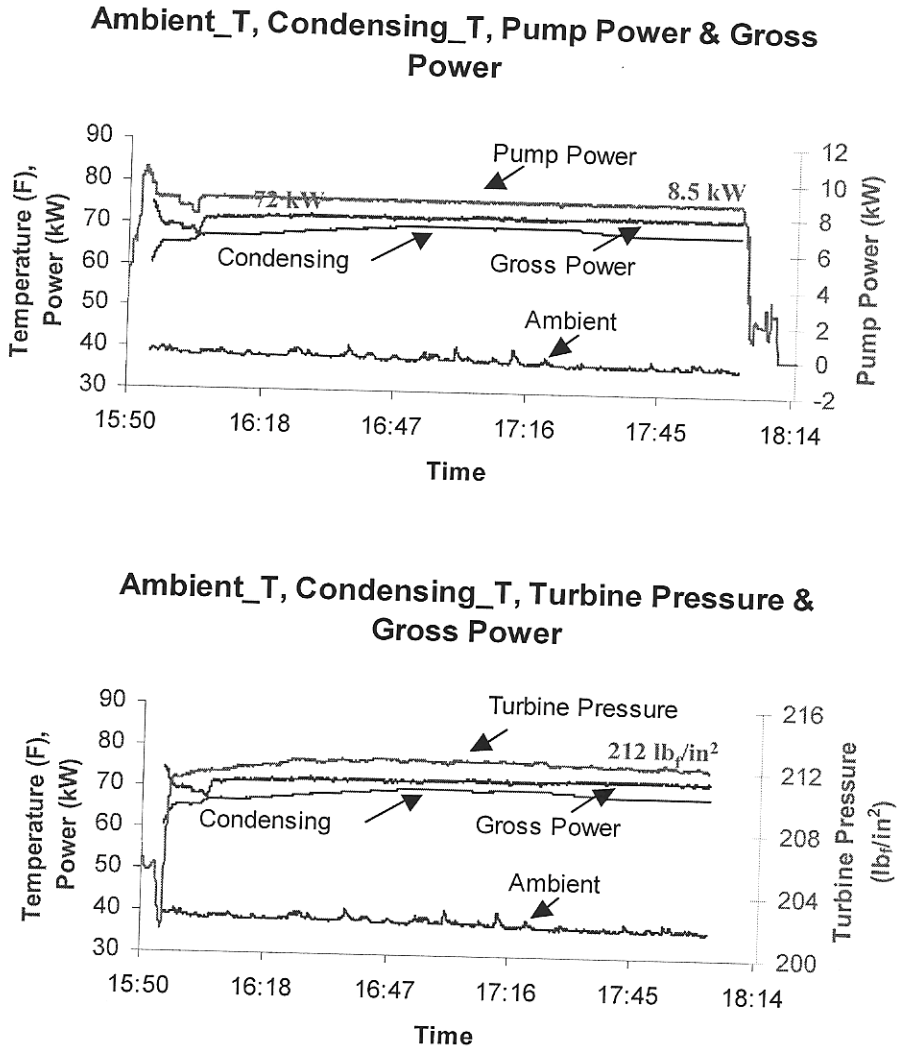

Figure 3.3.2 Measured ORC system performance with C200 exhaust

3.3.1 ORC Component Performance

Analyses were performed to determine whether each ORC component performed as predicted. Figure 3.3.3 and the following figures are aimed at answering just that question. The first curve of Figure 3.3.3 was a measure of ORC aerodynamic efficiency when the turbine was run in steady state. It shows an efficiency of 80 % at pressure ratio of 15.6 matching the prediction very well.

It was also desired to determine whether full predicted power would have been generated if the design point exhaust energy was delivered to the evaporator. In order to answer

this question, the ORC system was operated in a quasi-transient manner. The process involved deliberately starving the evaporator refrigerant in order to get the evaporator metal hotter. The refrigerant pump speed was initially reduced and then suddenly increased to full speed. By this method, the design point of a 300 lbf/in2 turbine inlet pressure was achieved for a quasi-steady period.

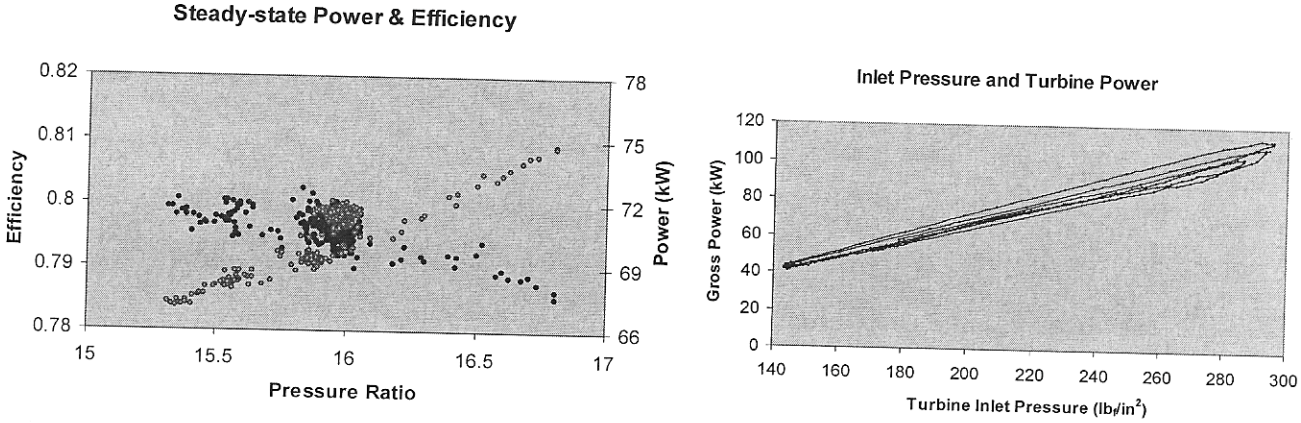

Figure 3.3.3 ORC performance characteristics (a) Steady (b) Quasi-steady

Figure 3.3.3b is the result of such measurement. The multiple curves show repeated quasi-steady periods of operation. Importantly, the ORC gross generated power was repeatedly measured as 110 kW for the 300 lbf/in2 inlet pressure condition. This value validated that the turbine design point performance was achieved.

Figure 3.3.4 is a plot of condenser heat rejection and the temperature difference between the leaving water temperature and the condenser saturation temperature. A small difference is a measure of good condenser performance and absence of non-condensibles in the condenser. Although the load 122 ton is 80% of the 153 ton design, the 2.2F difference is in line with the predicted 3F at the full load of 153F.

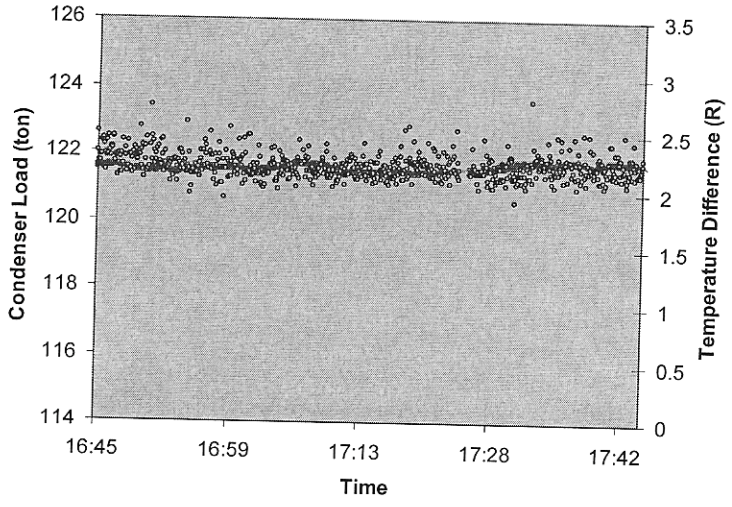

Figure 3.2.4 ORC condenser performance

The refrigerant pump performed according to the performance map, which was supplied by the manufacturer. The criterion for selecting the recuperator was to minimize gas side pressure drop. It was therefore over sized in terms of heat transfer by a factor of 2. Figure 3.2.5 shows that this minimal pressure drop was achieved.

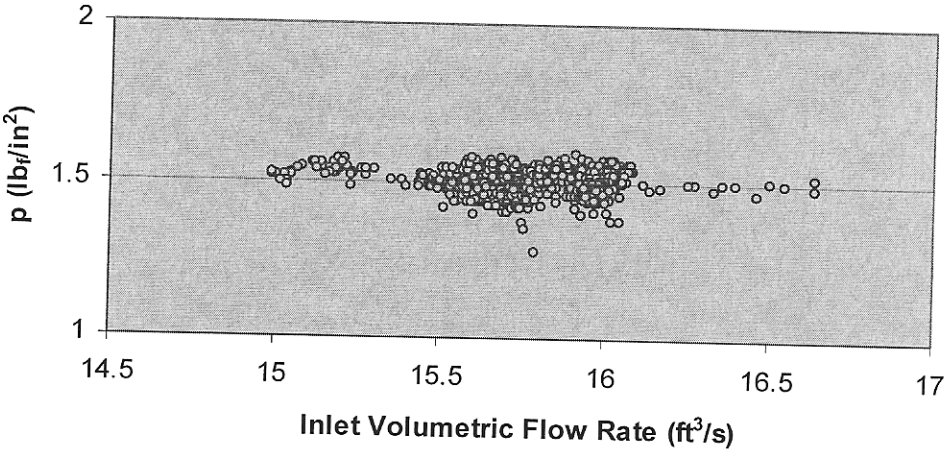

Figure 3.2.5 ORC recuperator pressure drop

Calculations were also was made using our model to predict the performance of the evaporator for the inlet condition of actual measured C200 exhaust temperature and gas flow rate. The evaporator exit temperature and total heat transfer predictions track with the actual measured values as shown in Figure 3.2.6.

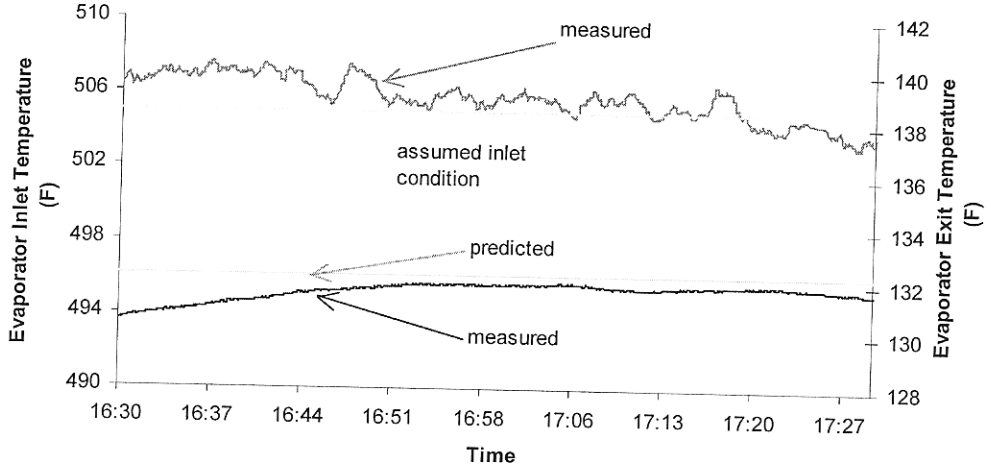

Figure 3.2.6 ORC evaporator performance

3.4 Integrated Advanced Microturbine System Performance

The results of analyses of data from the C200/ORC integrated system tests are shown in Table 3.3.1.

Table 3.3.1 Performance of C200/ORC Advanced Microturbine System

Parameter		Integrated System	
		Spec	Meas
Ambient Temperature	F	34	34
C200 Beta Backpressure	in H_2O	4	4
C200 Beta Power	kW	400	400
C200 Beta Electrical	%	32.3	32.8
ORC Power	kW	82.0	64.6
System Efficiency	%	38.9	38.0

The measured C200, ORC, and system data indicated that:

- With no backpressure, each C200 unit achieved an electrical efficiency of 33%. With the slight backpressure of the integrated system, the C200 electrical efficiency was reduced only to 32.8%.
- The ORC system and component performance matched or slightly exceed pre-test predictions enabling it to achieve a system electrical efficiency of 13%.
- The integrated system produced 400 kW from the two C200 units and an additional 64.6 kW from the ORC to achieve a system efficiency of 38.0% at a 34F ambient day.
- The integrated system produced less than the pre-test predicted efficiency of 38.9% because unplanned C200 cabinet cooling reduced the exhaust energy available to the ORC by ~ 12% of the fuel energy.